Supplementary Information

Bioinspired Pre-Programmable Pneumatic Actuator: Leveraging Mechanical Anisotropy of Nonwoven Fabrics with Integrated Tensile Sensor

Fabrication of the Actuator: The shell of the actuator was produced by cutting the nonwoven fabrics into 50 mm × 150 mm rectangle shape and sewing the sample into a 3D tube using the self-spun PET yarns. The flat seam was selected for sewing the tube because the stitches have low deformation along the sewn direction, and thus sewn-in PET yarn is leveraged as the strain limiting yarn to achieve bending actuation of fabricated actuator. Then a silicone bladder with diameter of 10 mm and length of 140 mm was inserted into the tube. The lids of plastic polylactic acid (PLA) for sealing the both ends of the bladder were manufactured using a 3D printer (Allcct-Mars2). The lids are glued to the bladder at the edge of the end and further tied with the knit tube by cable ties to avoid any possible air leakage.

Preparation of TPU-AgNW/Mxene sensor: AgNWs and MXene nanosheets were first respectively prepared following the procedure detailed in the previously reported work.[1, 2] Then, 0.1 g AgNWs and 0.1 g MXene were uniformly dispersed into 4 g DMF solution by sonication to form a suspension. Finally, 0.8 g TPU were added into the above suspensions and stirred for 6 h to obtain a homogenous wet-spinning solution. The spinning solution was extruded from a syringe at a speed of 80 mL/min through a spinneret (inner diameter: 460 μm) into an isopropanol-based coagulation bath. the coagulation solution was 30 vol % isopropanol in water. The surfactant and DMF were removed during the coagulation process, and the continuous fiber was taken up on an aluminum foil drum. Finally, the composite TPU-AgNW/Mxene fibers were obtained after dried for 2h at room temperature.

Characterization: The abrasion test was performed using Martindale Abrasion Tester (YG(B)401T, Wenzhou Darong Textile instrument Co.,Ltd, China).[3] The blocking force

of the actuator was measured by an electronic balance (FA2004N). A Meters CMT6103 tester (MET, USA) was used to measure the tensile properties of the nonwoven fabrics. In the tensile measurements, samples were clamped at a distance of 50 mm and stretched at a test speed of 50 mm min^{-1}. The trajectory of the actuator tip in the X, Y, and Z directions was captured by a set of digital cameras and drawn with the aid of Tracker software (Avanquest USA LLC). The experiments towards environmental characteristics were conducted by varying the test temperature and humidity using temperature/humidity controlling system (Siemens Co. Germany) with precision of ±0.5 °C and 1% RH, then the electromechanical properties in different temperatures and hunidity of the strain sensors were measured with semiconductor characterization system (Keithley DMM6500, Tektronix, USA). According to GB/T·12704.2-2009, the YG601H-II fabric moisture permeability testing apparatus is used to measure the water vapor permeability of the fabric.[4] Additionally, the morphology for MXene nanosheets are confirmed by transmission electron microscopy (TEM) measurement. The consent was obtained for the experiments involving human participants.

Formula calculation: Combining Eq. 1 with the Eqs. 3 and 4 for the length of an arc, the following equations can be formed to describe the length of the two opposite sides of the bending actuator:

$$L_0=2n\cdot b\cos(\theta_{max})=r_i\alpha \tag{S1}$$

$$L_n=2n\cdot b\cos(\theta)= r_o\alpha \tag{S2}$$

With the assumption that the cross section of actuator remains to be a perfect circle, the overall diameter will be the sum of the radii on the outside of the curve (r_1) and inside of the curve (r_2). Hence, Eq. 2 can be used to determine the diameter of the bent actuator:

$$r_1 = \frac{D_1}{2} = \frac{b\sin(\theta)}{2n\pi} - \frac{d}{2} \tag{S3}$$

$$r_2 = \frac{D_2}{2} = \frac{b\sin(\theta_{max})}{2n\pi} - \frac{d}{2} \tag{S4}$$

$$D_c = r_1 + r_2 \tag{S5}$$

$$D_c = \frac{b\sin\theta+b\sin\theta_{max}}{2n\pi} - d \tag{S6}$$

Using the above information, we can obtain the following equation about the

bending actuator. By substituting Eq. 4 in Eq. S2, we have,

$$L_n=(D_c+r_i)\,\alpha \tag{S7}$$

Through substituting Eqs. S1 and S2 into Eq. S7, we yield,

$$L_n = \left(D_c + \frac{L_0}{\alpha}\right)\alpha = D_c\alpha + L_0 = 2nbcos\theta \tag{S8}$$

The volume changes of the actuator induced by applied air pressure can increase the input work W_{in}, which can be described by the following equation,

$$dW_{in} = \int_{s_i} (P' - P_0)\, dl_i . ds_i = (P' - P_0) \int_{s_i} dl_i \,.\, ds_i = P.dV_c \tag{S9}$$

Where P' is the internal absolute air pressure, P_0 is the ambient pressure, P is the differential air pressure, s_i is the actuator inner surface, dl_i is the inner surface displacement vector, ds_i is the area vector, and dV_c is the actuator volume change.

Based on the cylinder volume formula,

$$V = \frac{\pi D^2 L}{4} \tag{S10}$$

The bended actuator volume V_c can be found as follows,

$$V_c = \frac{\pi D_c^2 L_c}{4} = \frac{b(cos\theta+cos\theta_{max})\left[b^2(sin\theta+sin\theta_{max})^2+4n^2\pi^2d^2-4n\pi db(sin\theta+sin\theta_{max})\right]}{8n\pi} \tag{S11}$$

Where D_c is the curved actuator diameter from Eq. (S6) and L_c is the central curved actuator length from Eq. (S8).

The output work W_{out} is associated with an increase in actuator length L_c because of the change in volume when the actuator bends. This can be described by the following equation,

$$dW_{out} = F.dL_c \tag{S12}$$

The output force can therefore be determined by combining Eqs. S9 and S12 as follows:

$$F = P\frac{dV_c}{dL_c} \tag{S13}$$

Differentiating with respect to θ gives:

$$\frac{dV_c}{d\theta} = \frac{b}{8n\pi}\{sin\theta(sin\theta + sin\theta_{max})[4ndb\pi - b(sin\theta + sin\,\theta_{max})^2] - 4n^2d^2\pi^2bsin\theta + (cos\theta + cos\theta_{max})(2b^2cos\theta sin\theta + 2b^2cos\theta sin\theta_{max} - 4ndb\pi cos\theta)\} \tag{S14}$$

and:

$$\frac{dL_c}{d\theta} = -nbsin\theta \tag{S15}$$

Because of the inserting of the two inelastic constrained wires, the NFPA possesses a strain gradient along radial direction to form a bending shape (Figure S6). Considering the bending moment equilibrium state of the NFPA after actuation, we obtain,

$$\int_0^{D_2} \sigma_l^{elastic} rJ(r)dr + \int_{-D_1}^{0} \sigma_l^{inelastic} rJ(r)dr = M/2 \tag{S16}$$

Where $J(r) = \sqrt{D_c r - r^2} - \sqrt{d_c r - r^2}$, $\sigma_l^{elastic}$ and $\sigma_l^{inelastic}$ represent the axial stresses in the elastic and inelastic regions, and can be estimated by,

$$\sigma_l^{elastic}(r)\Big|_{r>0} = \left(\frac{r}{\rho} + v\varepsilon_r\right)\frac{E_l^{low}}{1-v^2} \tag{S17}$$

$$\sigma_l^{inelastic}(r)\Big|_{r<0} = \left(\frac{r}{\rho} + v\varepsilon_r\right)\frac{E_l^{high}}{1-v^2} \tag{S18}$$

Substituting equations S17 and S18 into equation S16 and integrate the equation S1numerically based on the expansion of two-order Talor formula, we get,

$$2\kappa\left[Y(D_2)E_l^{elastic} + Z(D_1)E_l^{inelastic}\right] = \frac{M(1-v^2)}{1+v^2} \tag{S19}$$

Where $Y(D_2)=(D_c - d_c)\left(\frac{D_2^3}{6} + \frac{2D_2^5}{5D_c d_c}\right)$, $Z(D_1)=(D_c - d_c)\left(\frac{D_1^3}{6} + \frac{2D_1^5}{5D_c d_c}\right)$

By referring to the geometrical relationship in Figure S6, we obtain,

$$\cos\varphi = \frac{D_2 - D_1}{D_1 + D_2} \tag{S20}$$

Therefore, uniting the equations S19 and S20, we can reveal the the relationship between the bending curvture κ and relative axial angles (φ).

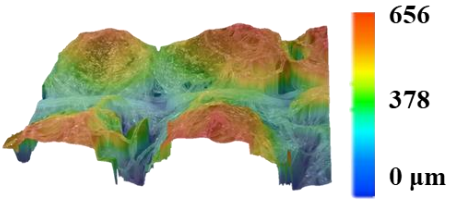

Figure S1. Three-dimensional confocal laser microscopy images of elastic nonwoven fabric

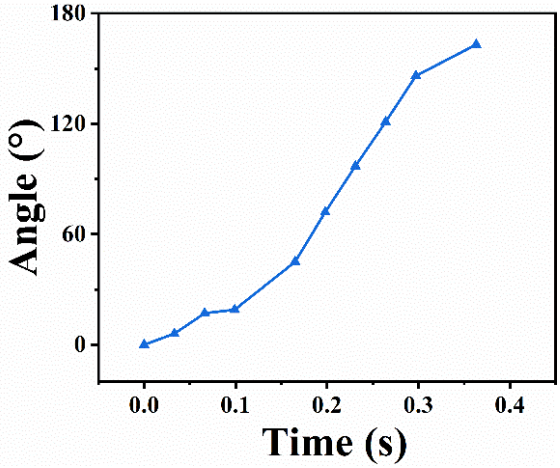

Figure S2. The correlation between bending angle and response time for NFPA-0.

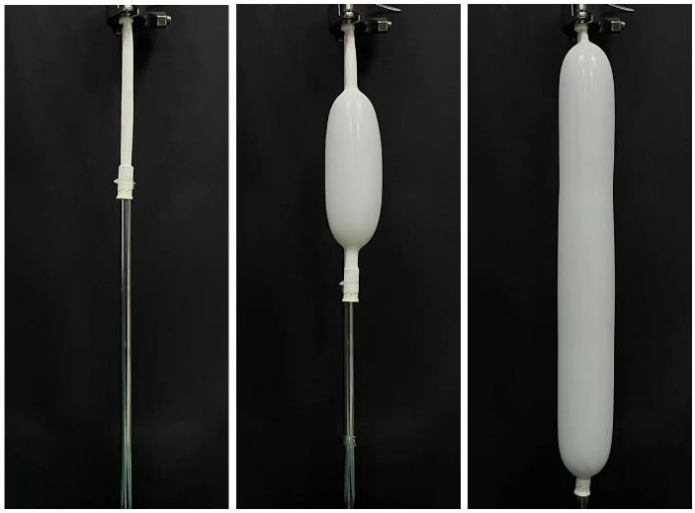

Figure S3. Dilatometric change of bare silicone bladder

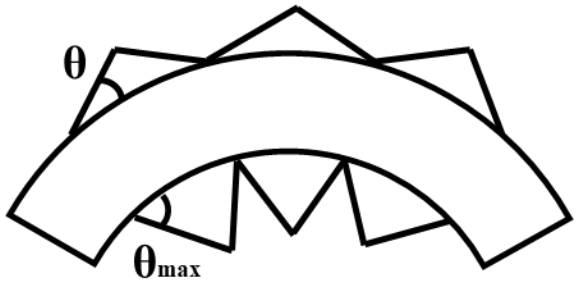

Figure S4. Bending angle diagram of NFPA.

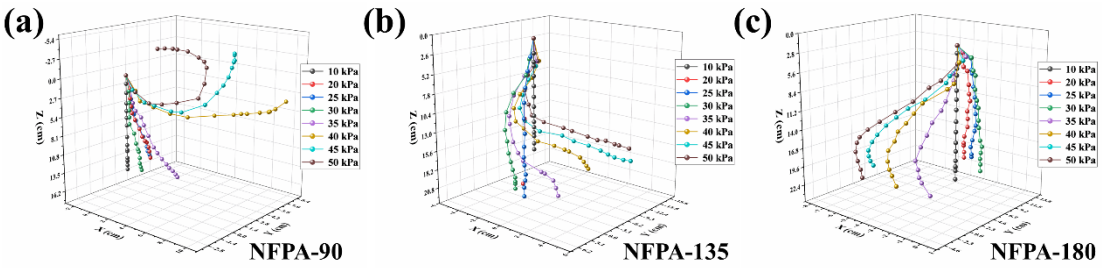

Figure S5. Multi-mode motion of (a) NFPA-90, (b) NFPA-135 and (c) NFPA-180 with unit vector trajectory in a spatial coordinate (pressure range: 10-50 kPa).

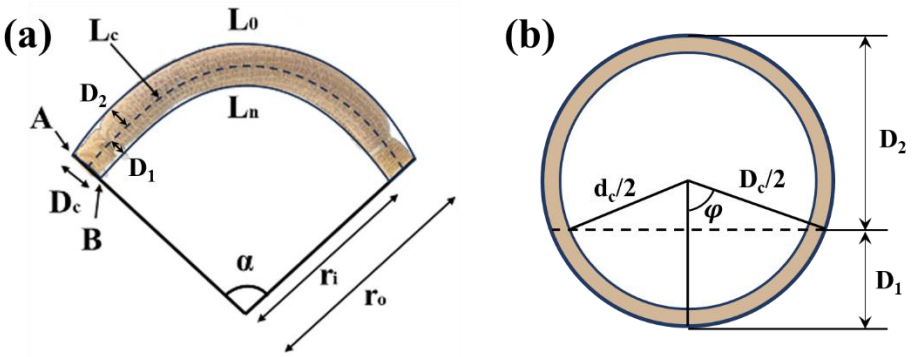

Figure S6. Schematic illustration of the geometrical structure of the longitudinal section (a) and cross section (b) of the NFPA.

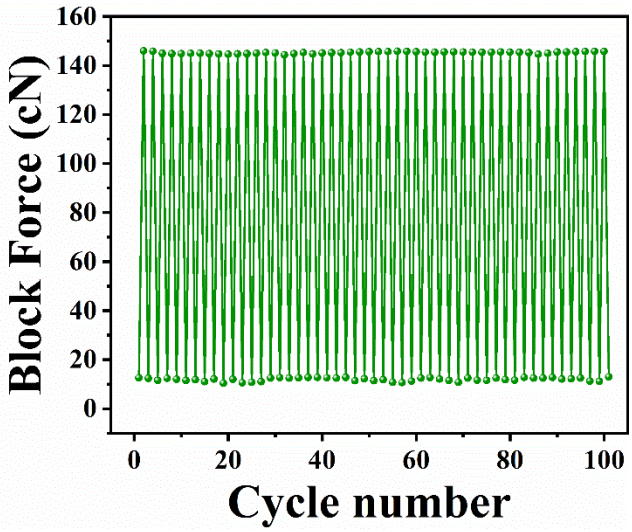

Figure S7. Block force output of NFPA-90 under 100 reversible cyclic after 10 days of aging treatment

Figure S8. Optical photograph of conductive sensing fiber.

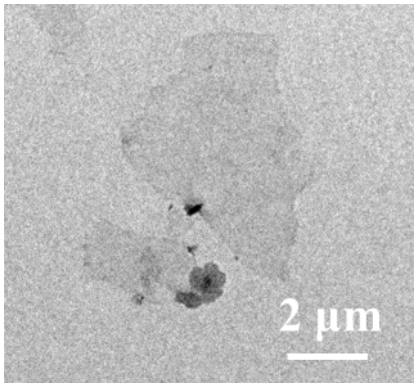

Figure S9. Transmission electron microscopy image of MXene ($Ti_3C_2T_X$) nanosheets.

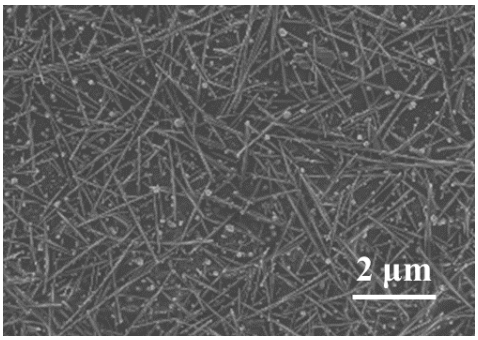

Figure S10. Scanning electron microscope image of AgNWs.

References

1. S. Li, D. Liu, N. Tian, Y. Liang, C. Gao, S. Wang, and Y. Zhang, *Mater. Today Commun.*, 2019, **20**, 100546.
2. C. Lan, H. Jia, M. Qiu, and S. Fu, *ACS Appl. Mater. Interfaces*, 2021, **13**, 38761-38772.
3. M. Uzun, K. Govarthanam, S. Rajendran, and E. Sancak, *Wear*, 2015, **322**, 10-16.
4. P. Gu, N. Fan, Y. Wang, J. Wang, P. Müller-Buschbaum, and Q. Zhong, *ACS Appl. Mater. Interfaces*, 2019, **11**, 30269-30277.